Int J Adv Manuf Technol (2009) 42:250–262
DOI 10.1007/s00170-008-1601-7

ORIGINAL ARTICLE

Laser shock processing: modeling of evaporation and pressure field developed in the laser-produced cavity

B. S. Yilbas · S. B. Mansoor · A. F. M. Arif

Received: 6 December 2007 / Accepted: 4 June 2008 / Published online: 26 July 2008

Abstract Laser shock processing during high-intensity beam ablation of the metallic surface is examined. The phase change due to evaporation and melting is modeled using an energy method. The vapor front expansion and pressure build-up in the laser-produced cavity are obtained numerically using a control volume approach. Elasto-plastic response of the substrate material due to mechanical loading of pressure field developed in the cavity is modeled and predicted using a finite element method. It is found that a high-pressure region is developed in the vicinity of the cavity edge, which, in turn, results in excessive stresses and plastic strain in this region. The depth of the plastic region in the order of a few micrometers below the surface is predicted.

Keywords Laser · Shock · Cavity · Evaporation

1 Introduction

Laser shock processing of metallic surfaces provides rapid surface hardening through dislocation and phase formations in the vicinity of the surface process. The depth of the laser-processed zone depends mainly on the laser power intensity, pulse length, and material properties. In this case, rapid evaporation of the surface under high-intensity radiation results in high values of recoil pressure across the ablated surface. As the vapor front expands into its surrounding ambient while solid surface recesses towards the bulk, the considerably high pressure is generated across the vapor front and the recessing surface due to momentum change in this region. The liquid ejection from the irradiated surface does not take place during the evaporation process due to short heating duration (a few nanoseconds) [1]. Moreover, thermal separation of electron and lattice sub-systems during the rapid heating of the surface does not occur. This is due to the fact that the nanosecond heating duration is considerably higher than the electron relaxation time [2]. However, a model study of laser shock processing gives insight into the physical processes taking place in the irradiated region. Consequently, investigation into a laser shock processing allowing the phase change and recessing surface in the irradiated region becomes necessary. This, in turn, provides improved understanding of the laser shock processing.

Considerable research studies were carried out to examine the laser shock processing. A review of laser shock processing and examination of microstructural changes in the laser-irradiated region was carried out by Montross et al. [3]. They indicated that laser shock processing had great potential as a means of improving the mechanical performance of components. The model study on laser shock processing was carried out by Thorslund et al. [4]. They showed that pulses with short rise times yielded higher plasma pressure. A model study on laser-induced shock wave propagation was carried out by Senecha et al. [5]. They demonstrated that the simulation could be used as an effective tool for benchmark calculation of laser absorption coefficients. Multiple laser shock processing was modeled by Ding and Ye [6]. They evaluated the effect of pressure magnitude and duration on the compressive stress field in the metallic substrate. Yin et al. [7] examined laser shock processing. They developed a five-axis work table for efficient processing. Laser shock

B. S. Yilbas (✉) · S. B. Mansoor · A. F. M. Arif
ME Department, KFUPM,
Dhahran 31261, Saudi Arabia
e-mail: bsyilbas@kfupm.edu.sa

processing in water confinement regime was investigated by Berthe et al. [8]. They showed that laser power density transmitted through the plasma was limited at 10 GW/cm^2. Laser-induced plasma shock wave was investigated by Chen et al. [9]. They developed an optical deflection system to detect laser-induced plasma shock waves, cavitation bubbles, and second collapse shock waves in water. Laser-induced shock wave formation and laser-induced damage were investigated by Faraggi et al. [10]. They showed that the peak pressure varied slowly as a function of laser pulse duration; however, as the pulse length is shortened below the confinement time, a shock was produced. High-intensity laser shock processing was carried out by Schmidt-Uhlig et al. [11]. They indicated that the shock-affected depth in the order of 100 μm was achieved. The recoil pressure generated in the irradiated region was examined by Zhang et al. [12]. They measured the complete shape of pressure pulse and the peak pressures at the back face of the workpiece during laser shock processing. The model and experimental studies on laser shock processing were carried out in the previous studies [13]. However, the model studies were limited to the equilibrium assumption at the vapor–liquid interface; in which case, all the laser energy was absorbed at the workpiece surface during the ablation process. However, laser energy is absorbed within the absorption depth in the substrate material with decreasing intensity (Lambert's law). Consequently, when modeling rapid evaporation process, this effect should be accommodated.

In the present study, a model study for the laser shock processing is carried out and phase changes due to melting and evaporation are accommodated for volumetric laser heat source (employing decaying pulse energy intensity with depth). Recession of the solid surface and formation of mushy zones are predicted using a numerical method employing a finite difference scheme while recoil pressure and evaporating front velocity are obtained using the control volume approach via solving the flow equations. The stress fields in the laser-shock-affected region are predicted using a finite element method.

2 Mathematical modeling of phase-change processes

The Fourier heating model is used to obtain temperature distribution in each phase. The energy method is used to determine the mushy zones where two phases mutually exist. In the analysis, the laser output power intensity is considered as Gaussian, and its centre is located at the centre of the co-ordinate system adopted. This arrangement results in an axisymmetric heating of the workpiece material. The time exponentially varying laser pulse is used in the simulations. The heat conduction equation for laser heating in solid phase due to a Gaussian intensity profile of laser output power can be written as:

$$\rho_s c_{p_s} \frac{\partial T}{\partial t} = \frac{k_s}{r} \frac{\partial}{\partial r}\left(r \frac{\partial T}{\partial r}\right) + k_s \frac{\partial^2 T}{\partial z^2} + S_o \tag{1}$$

where S_o is the volumetric source term and it is in the form of,

$$S_o = I_0(t)\delta(1 - rf)\exp(-\delta z)\exp\left(-\frac{r^2}{a^2}\right)$$

$I_{0(t)}$, δ, r_f and a are the laser peak power intensity, absorption coefficient, reflectivity, and the Gaussian parameter, respectively.

The substrate material is assumed initially at a uniform temperature, T_o, i.e.:

$$\text{At time zero} \Rightarrow t = 0 : T(r,z,0) = T_o (\text{which is specified})$$

Laser heating is assumed to have no effect on the temperature rise at a depth of infinity below the surface; therefore, temperature is assumed to be constant and equals to the initial temperature of the substrate material at this depth. The boundary conditions are:

$$r \text{ at infinity} \Rightarrow r = \infty : T(\infty, z, t) = T_o \text{ (specified)}$$

$$z \text{ at infinity} \Rightarrow r = \infty : T(r, \infty, t) = T_o \text{ (specified)}$$

At the symmetry axis, temperature reaches maximum and the convection boundary condition is considered at the workpiece surface, i.e.:

$$\text{At symmetry axis} \Rightarrow r = 0 : \frac{\partial T(0,z,t)}{\partial r} = 0$$

and

$$\text{At the surface} \Rightarrow z = 0 : k\frac{\partial T(r,0,t)}{\partial z} = h(T(r,0,t) - T_o)$$

where h is taken as 10 W/m^2 K due to natural convection from the surface.

The evaporation temperature depends on the vapor pressure; however, pressure-dependent evaporation temperature is not known in the open literature for steel vapor. Therefore, it is assumed that the substrate material has single melting and boiling temperatures. A mushy zone (mutual existence of two phases) is developed across the interface of two phases, once the phase change initiates. During the phase-change process, enthalpy changes while temperature of the substrate material remains the same in the mushy zone. Moreover, the nominal laser pulse length employed in the analysis is 24 ns, therefore, the flow in the vapor and liquid layer during the heating process can be neglected. Consequently, during the short heating period,

the fluid motion in the liquid and vapor layers is assumed to have no effect on the heat transfer mechanism in these zones. Mass fraction of species content in the mushy zone can be formulated via energy balance in the mushy zone. The energy equation for the differential element in the mushy zone [14]:

$$\rho_{\mathrm{m}} L_{\mathrm{m}} \frac{\partial x_{\mathrm{m}}}{\partial t} = \frac{k_{\mathrm{m}}}{r} \frac{\partial}{\partial r}\left(r \frac{\partial T}{\partial r}\right) + k_{\mathrm{m}} \frac{\partial^2 T}{\partial z^2} + S_{\mathrm{o}} \tag{2}$$

where x_{m} is the mass fraction of the liquid phase in the mushy zone, i.e.:

$$x_{\mathrm{m}} = \frac{m_{\mathrm{m}}}{m_{\mathrm{m}} + m_{\mathrm{s}}}$$

Equation (2) is valid in the mushy zone where $0 \leq x_{\mathrm{m}} \leq 1$, i.e., temperature of the cells with $0 \leq x_{\mathrm{m}} \leq 1$ is set to melting temperature ($T = T_{\mathrm{m}}$). For the situation $x_{\mathrm{m}} = 1$, liquid phase occurs and Eq. (1) is used to determine the temperature rise in the liquid heating while using the liquid thermal properties in the equation. Moreover, the liquid heating continues until the boiling point is reached in the substrate material, in which case, a new mushy zone is formed. In this case, Eq. (2) is modified for a differential element in the mushy zone subjected to evaporation [15], i.e.:

$$\rho_{\mathrm{b}} L_{\mathrm{b}} \frac{\partial x_{\mathrm{b}}}{\partial t} = \frac{k_{\mathrm{b}}}{r} \frac{\partial}{\partial r}\left(r \frac{\partial T}{\partial r}\right) + k_{\mathrm{b}} \frac{\partial^2 T}{\partial z^2} + S_{\mathrm{o}} \tag{3}$$

where x_{b} mass fraction of vapor phase in the mushy zone, i.e.:

$$x_{\mathrm{b}} = \frac{m_{\mathrm{b}}}{m_{\mathrm{m}} + m_{\mathrm{b}}}$$

Equation (3) is applicable for temperature $T = T_{\mathrm{b}}$ and $0 \leq x_{\mathrm{b}} \leq 1$ in the mushy zone (partially liquid partially vapor zone); in which case, temperature of the cells with $0 \leq x_b \leq 1$ is set to the boiling temperature of the substrate material ($T = T_{\mathrm{b}}$). It should be noted that x_{m} is replaced with x_{b} in Eq. (3), which represents the fraction of vapor phase in the differential element. The calculation of x_{b} is the same as x_{m}, provided that latent heat of fusion is replaced with latent heat of evaporation of the substrate material in Eq. (3) in the latter.

The boundary condition at the evaporating surface is introduced in relation to Eq. (63). In this case, the temperature along the evaporated surface is kept at boiling temperature of the substrate material, i.e., the cells in the evaporated region are kept at boiling temperature, i.e.:

In the mushy zone, at $z = z_{\mathrm{b}} \Rightarrow T(r, z_{\mathrm{b}}, t) = T_{\mathrm{b}}$, where z_{b} represents the axial location at the evaporated surface.

Equations (2) and (3) provide the relative position of solid–liquid and liquid–vapor interface in the substrate material. Liquid–vapor interface determines the shape and size of the cavity generated during the evaporation process.

3 Transiently developing vapor jet

The vapor front emerging from the laser-induced cavity is modeled numerically using a control volume approach. The laser-produced cavity shape and its temporal progression as predicted from the finite difference scheme are employed in the simulations. In this case, the time-varying cavity shape, mass flux of the vapor and the temperature distribution at the cavity surface are the inputs for the simulations of the flow filed due to vapor jet emanating from the cavity. In the flow analysis, the time-averaged conservation equations are accommodated for an unsteady, incompressible, axisymmetric turbulent flow situation resembling the vapor jet expansion. The standard k–ε turbulence model is used to account for the turbulence. Moreover, the species transport model is also used to account for the mass transfer of the vapor jet from the cavity into the stagnant water ambient. It should be noted that all the unknown quantities are time-averaged since the RANS equations are used.

3.1 Continuity equation

The conservation of mass in the cylindrical coordinates for compressible transient flow situation can be written as:

$$\frac{1}{r}\frac{\partial(\rho r V_{\mathrm{r}})}{\partial r} + \frac{\partial(\rho V_{\mathrm{z}})}{\partial r} + \frac{\partial \rho}{\partial t} = 0 \tag{4}$$

3.2 Radial momentum

The vapor emanating from the cavity has the radial momentum. Since the flow expansion takes place at high velocities, the flow field becomes turbulent. This requires accommodating the turbulence model. In this case, the k–ε turbulence model is used to account for the turbulence. The momentum conservation in the radial direction for compressible transient turbulent flow situation can be written as:

$$\begin{aligned}\frac{\partial(\rho V_r)}{\partial t} + \frac{1}{r}\frac{\partial\left(\rho r V_r^2\right)}{\partial r} + \frac{\partial(\rho V_r V_z)}{\partial z} &= -\frac{\partial p}{\partial r} \\ &+ \frac{2}{r}\frac{\partial}{\partial r}\left(\mu_{\mathrm{eff}} r \frac{\partial V_r}{\partial r}\right) + \frac{\partial}{\partial z}\left(\mu_{\mathrm{eff}} \frac{\partial V_r}{\partial z}\right) \\ &+ \frac{\partial}{\partial z}\left(\mu_{\mathrm{eff}} \frac{\partial V_z}{\partial z}\right) - 2\mu_{\mathrm{eff}} \frac{V_r}{r^2}\end{aligned} \tag{5}$$

3.3 Axial momentum

The axial momentum of the vapor can be written after considering the compressible transient turbulent flow situation, i.e.:

$$\begin{aligned}&\frac{\partial(\rho V_z)}{\partial t}+\frac{1}{r}\frac{\partial(\rho r V_r V_z)}{\partial r}+\frac{\partial\left(\rho V_z^2\right)}{\partial z}\\&=-\frac{\partial p}{\partial z}+\frac{1}{r}\frac{\partial}{\partial r}\left(\mu_{\text{eff}} r\frac{\partial V_z}{\partial r}\right)\\&\quad+2\frac{\partial}{\partial z}\left(\mu_{\text{eff}}\frac{\partial V_z}{\partial z}\right)+\frac{1}{r}\frac{\partial}{\partial r}\left(\mu_{\text{eff}} r\frac{\partial V_r}{\partial z}\right)\end{aligned}\tag{6}$$

where, μ_{eff} is the effective viscosity, which is $\mu_{\text{eff}}=\mu+\mu_{\text{t}}$ and

$$\mu_{\text{t}}=\frac{\rho C\mu K^2}{\varepsilon}:C_\mu=0.09$$

μ_{t} is the turbulence viscosity, μ is the bulk viscosity of the vapor, and K is the turbulence kinetic energy generation.

3.4 Energy equation

Since the flow due to the vapor expansion from the cavity is turbulence and the vapor front expands into the stagnant water, the energy equation for the flow filed should contain the species (vapor and water) transport of energy. In this case, the resulting energy equation becomes:

$$\begin{aligned}&\frac{\partial(\rho E)}{\partial t}+\frac{1}{r}\frac{\partial(rV_r\rho E)}{\partial r}+\frac{\partial(V_z\rho E)}{\partial z}\\&=\frac{1}{r}\frac{\partial}{\partial r}\left(rk_{\text{eff}}\frac{\partial T}{\partial r}\right)+\frac{\partial}{\partial z}\left(k_{\text{eff}}\frac{\partial T}{\partial z}\right)\\&\quad+\left[\frac{1}{r}\frac{\partial}{\partial r}\left(rh_{\text{vapor}}\left(\rho D+\frac{\mu_{\text{t}}}{Sc_{\text{t}}}\right)\frac{\partial Y_{\text{vapor}}}{\partial r}\right)+\frac{\partial}{\partial z}\left(h_{\text{vapor}}\left(\rho D+\frac{\mu_{\text{t}}}{Sc_{\text{t}}}\right)\frac{\partial Y_{\text{vapor}}}{\partial z}\right)\right]\\&\quad+\left[\frac{1}{r}\frac{\partial}{\partial r}\left(rh_{\text{water}}\left(\rho D+\frac{\mu_{\text{t}}}{Sc_{\text{t}}}\right)\frac{\partial Y_{\text{water}}}{\partial r}\right)+\frac{\partial}{\partial z}\left(h_{\text{water}}\left(\rho D+\frac{\mu_{\text{t}}}{Sc_{\text{t}}}\right)\frac{\partial Y_{\text{water}}}{\partial z}\right)\right]\end{aligned}\tag{7}$$

where, $E=Y_{\text{water}}h_{\text{water}}+Y_{\text{vapor}}h_{\text{vapor}}$, after neglecting the contribution of kinetic energy. Enthalpy of vapor and water are:

$$h_{\text{vapor}}=\int_{T_{\text{ref}}}^{T}\text{Cp}_{\text{vapor}}\,dT=\text{Cp}_{\text{vapor}}(T-T_{\text{ref}})\tag{8}$$

$$h_{\text{water}}=\int_{T_{\text{ref}}}^{T}\text{Cp}_{\text{water}}\,dT=\text{Cp}_{\text{water}}(T-T_{\text{ref}})\tag{9}$$

In Eqs. (4)–(6), the properties and parameters are:

$$k_{\text{eff}}=k+k_{\text{t}}:k_{\text{t}}=\text{Cp}\frac{\mu_t}{\text{Pr}_{\text{t}}}\text{ and }D=2.88\times10^{-5}\left(\text{m}^2/\text{s}\right)$$
$$:Sc_{\text{t}}=0.7:\text{Pr}_t=0.85:\text{T}_{\text{ref}}=298.15\text{K}$$

3.5 Turbulence kinetic energy equation, K

Since the flow is turbulence, turbulence kinetic energy generation can be modeled using the kinetic energy transport equation, which yields:

$$\begin{aligned}&\frac{\partial(\rho K)}{\partial t}+\frac{1}{r}\frac{\partial(\rho r V_r K)}{\partial r}+\frac{\partial(\rho V_z K)}{\partial z}\\&=\frac{1}{r}\frac{\partial}{\partial r}\left(\frac{\mu_{\text{eff}}}{\sigma_K}r\frac{\partial K}{\partial r}\right)+\frac{\partial}{\partial z}\left(\frac{\mu_{\text{eff}}}{\sigma_K}\frac{\partial K}{\partial z}\right)-\rho\varepsilon+P_K\end{aligned}\tag{10}$$

where,

$$P_K=\mu_{\text{eff}}\left[2\left\{\left(\frac{\partial V_z}{\partial r}\right)^2+\left(\frac{\partial V_r}{\partial r}\right)^2+\left(\frac{V_r}{r}\right)^2\right\}+\left(\frac{\partial V_z}{\partial r}+\frac{\partial V_r}{\partial z}\right)^2\right]$$

3.6 Rate of dissipation equation, ε

The turbulence kinetic energy dissipation is assumed to be of the same magnitude as the turbulence kinetic energy generation. Therefore, transport equation for the turbulence dissipation can be written as:

$$\begin{aligned}&\frac{\partial(\rho\varepsilon)}{\partial t}+\frac{1}{r}\frac{\partial(\rho r V_r\varepsilon)}{\partial r}+\frac{\partial(\rho V_z\varepsilon)}{\partial z}\\&=\frac{1}{r}\frac{\partial}{\partial r}\left(\frac{\mu_{\text{eff}}}{\sigma_\varepsilon}r\frac{\partial\varepsilon}{\partial r}\right)+\frac{\partial}{\partial z}\left(\frac{\mu_{\text{eff}}}{\sigma_\varepsilon}\frac{\partial\varepsilon}{\partial z}\right)\\&\quad-C_1\frac{\varepsilon}{K}P_K-C_2\rho\frac{\varepsilon^2}{K}\end{aligned}\tag{11}$$

where,

$$P_K=\mu_{\text{eff}}\left[2\left\{\left(\frac{\partial V_z}{\partial r}\right)^2+\left(\frac{\partial V_r}{\partial r}\right)^2+\left(\frac{V_r}{r}\right)^2\right\}+\left(\frac{\partial V_z}{\partial r}+\frac{\partial V_r}{\partial z}\right)^2\right]$$

and

$$\sigma_K=1\ \ \sigma_\varepsilon=1.3\ C_1=1.44\ C_2=1.92$$

3.7 Species transport equation

It is considered that the vapor front expands into the stagnant water resulting in the mixing of vapor and the water in the region above the laser-produced cavity surface.

This requires the transport equation of vapor to be considered, i.e.:

$$\frac{\partial(\rho Y_{\text{vapor}})}{\partial t}+\frac{1}{r}\frac{\partial(rV_r\rho Y_{\text{vapor}})}{\partial r}+\frac{\partial(V_z\rho Y_{\text{vapor}})}{\partial z} = \left[\frac{1}{r}\frac{\partial}{\partial r}\left(r\left(\rho D+\frac{\mu_t}{Sc_t}\right)\frac{\partial Y_{\text{vapor}}}{\partial r}\right)+\frac{\partial}{\partial z}\left(\left(\rho D+\frac{\mu_t}{Sc_t}\right)\frac{\partial Y_{\text{vapor}}}{\partial z}\right)\right] \quad (12)$$

Provided that the species balance yields:

$Y_{\text{water}} = 1 - Y_{\text{vapor}}$.

3.8 Initial and boundary conditions

Figure 1a shows the solution domain. It should be noted that the laser-produced cavity recesses towards the solid material while the evaporated front expands into the stagnant water during the heating period. This results in temporarily extending cavity and the vapor front expanding from the cavity. In this case, the solution domain evolves with time and moving cavity surface should be accommodated at the interface of liquid and vapor phases during the heating period. This situation is considered in Fig. 1a.

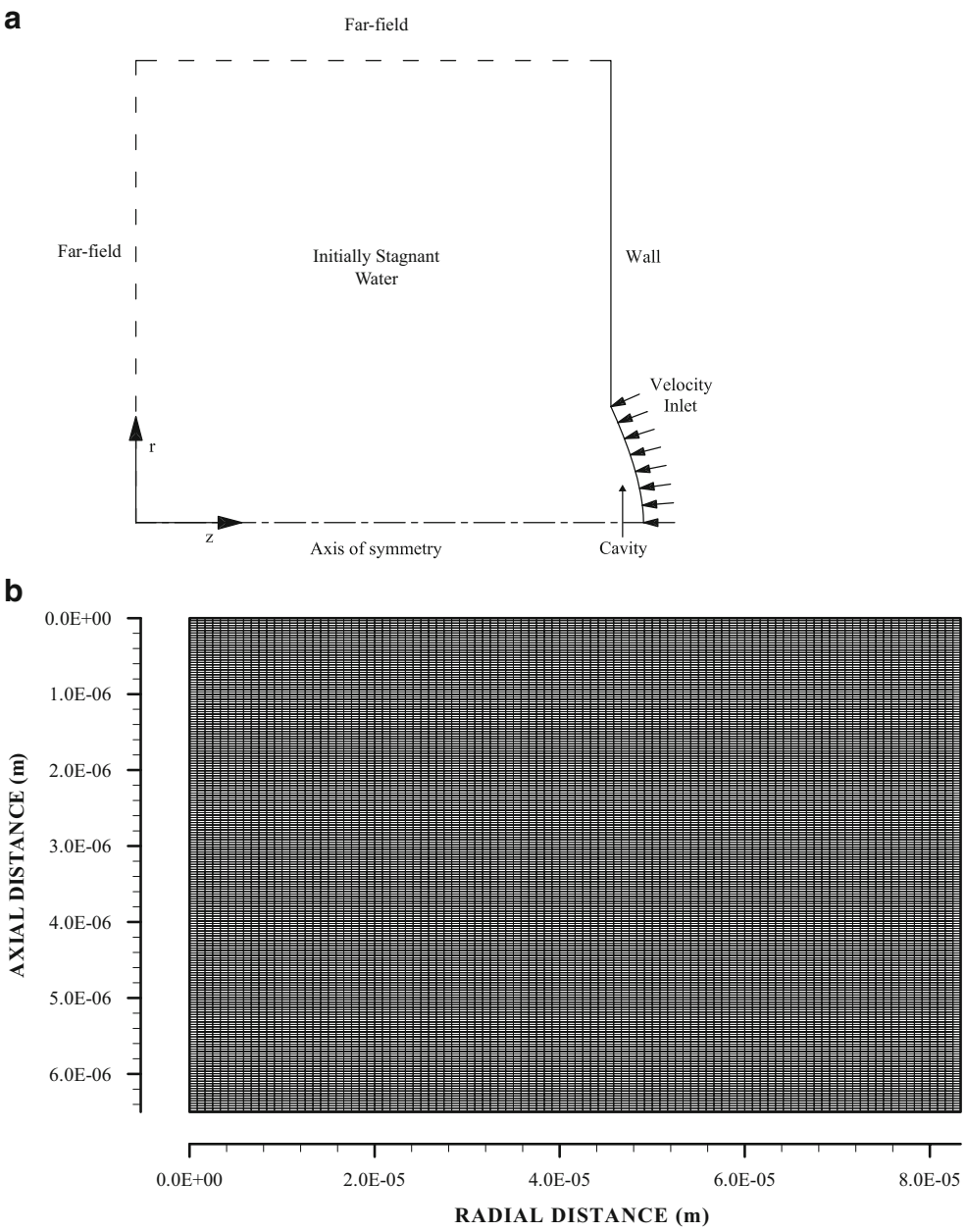

Fig. 1 **a** Solution domain of vapor jet emanating from cavity. **b** Solution domain of laser heated workpiece and used in the solid heating as well as mushy zone analysis while (0, 0) represents the irradiated spot center

Table 1 Thermal properties of steel used in the simulations

T_m (K)	T_b (K)	ρ (kg/m^3)	Cp (J/kg/K)	k (W/mK)	δ (1/m)	L_m (J/kg)	L_b (J/kg)
1,810	3,134	7,860	420	63	6.17×10^6	247,112	6,213,627

3.9 Symmetry axis: (r=0)

At the symmetry axis, all the unknown quantities are considered to be maximum accept the r-direction velocity, which is zero, i.e., for all z values and r=0 (symmetry axis), the boundary conditions are:

$$\left.\frac{\partial V_z}{\partial r}\right|_{\substack{z=z\\r=0}} = 0 : V_r(z,0) = 0 : \left.\frac{\partial T}{\partial r}\right|_{\substack{z=z\\r=0}} = 0 : \left.\frac{\partial K}{\partial r}\right|_{\substack{z=z\\r=0}} = 0 : \left.\frac{\partial \varepsilon}{\partial r}\right|_{\substack{z=z\\r=0}} = 0 : \left.\frac{\partial Y_{\text{vapor}}}{\partial r}\right|_{\substack{z=z\\r=0}} = 0$$

4 Far-field (outflow): At z=0

At the outflow boundary perpendicular to the z-axis the normal derivatives of all the unknown quantities are considered to be zero accept the r-direction velocity, whose value is zero as required from the continuity equation, i.e., for all r values and z=0 (at the free surface), the boundary conditions are:

$$\left.\frac{\partial V_z}{\partial r}\right|_{\substack{z=0\\r=r}} = 0 : V_r(0,r) = 0 : \left.\frac{\partial T}{\partial z}\right|_{\substack{z=0\\r=r}} = 0 : \left.\frac{\partial K}{\partial r}\right|_{\substack{z=0\\r=r}} = 0 : \left.\frac{\partial \varepsilon}{\partial r}\right|_{\substack{z=0\\r=r}} = 0 : \left.\frac{\partial Y_{\text{vapor}}}{\partial r}\right|_{\substack{z=0\\r=r}} = 0$$

4.1 Far-field (outflow): At r=r_{max}

At the outflow boundary perpendicular to the r-axis the normal derivatives of all the unknown quantities are considered to be zero accept the z-direction velocity, whose value is zero as required from the continuity equation, i.e., for all z values and r=r_{max} (radial location far away from the symmetry axis), the boundary conditions are:

$$V_z(z,r_{\max}) = 0 : \left.\frac{\partial V_r}{\partial r}\right|_{\substack{z=z\\r=r_{\max}}} = 0 : \left.\frac{\partial K}{\partial r}\right|_{\substack{z=z\\r=r_{\max}}} = 0 : \left.\frac{\partial \varepsilon}{\partial r}\right|_{\substack{z=z\\r=r_{\max}}} = 0 : \left.\frac{\partial Y_{\text{vapor}}}{\partial r}\right|_{\substack{z=0\\r=r_{\max}}} = 0$$

4.2 Solid wall: z=f(r,t)

The surface of the substrate material including the cavity surface acts like a solid wall in the solution domain and hence a no-slip and no-temperature-jump boundary conditions are considered. At the cavity surface, the vapor mass fraction is considered to be one whereas the water mass fraction is considered to be zero. Once the cavity profile in axial and radial directions is obtained from the numerical scheme (Eqs. (2) and (3)) for each time step, an algebraic equation is introduced, using the polynomial fitting technique, to resemble the temporal behavior of the cavity shape through using the computed data available for time steps. The vapor mass flow generated from the cavity surface recession during heating period is considered as the source of the mass of the vapor jet emanating from the cavity surface. The details of the analysis are given in [16].

4.3 Initial condition (t=0)

Initially, the ambient water is assumed as stagnant; therefore, the z and r-directions velocity components are zero. Initially, temperature is considered to be uniform and equal to 300 K in water ambient and the vapor mass fraction is zero whereas the water mass fraction is one throughout the domain.

5 Numerical solution

The numerical solution has two parts. In the first part, finite difference scheme used for the phase-change process (Eqs. (1), (2), and (3)) is introduced while in the second part, numerical solution for the flow equations is presented.

5.1 Phase-change process

Equation (1) is applicable to solid and liquid heating, Eq. (2) is applicable to mushy zone at solid–liquid interface and Eq. (3) is applicable to mushy zone at the liquid–vapor interface. To discretize the governing equations, a finite difference scheme is introduced. The details of the numerical scheme are given in [17]. To compute the equations discretized for temperature field and relative

Table 2 Laser pulse intensity used in the simulations

Peak intensity (W/m^2)	Gaussian parameter (1/m)	Nominal pulse length (ns)
9×10^{12}	120,000	24

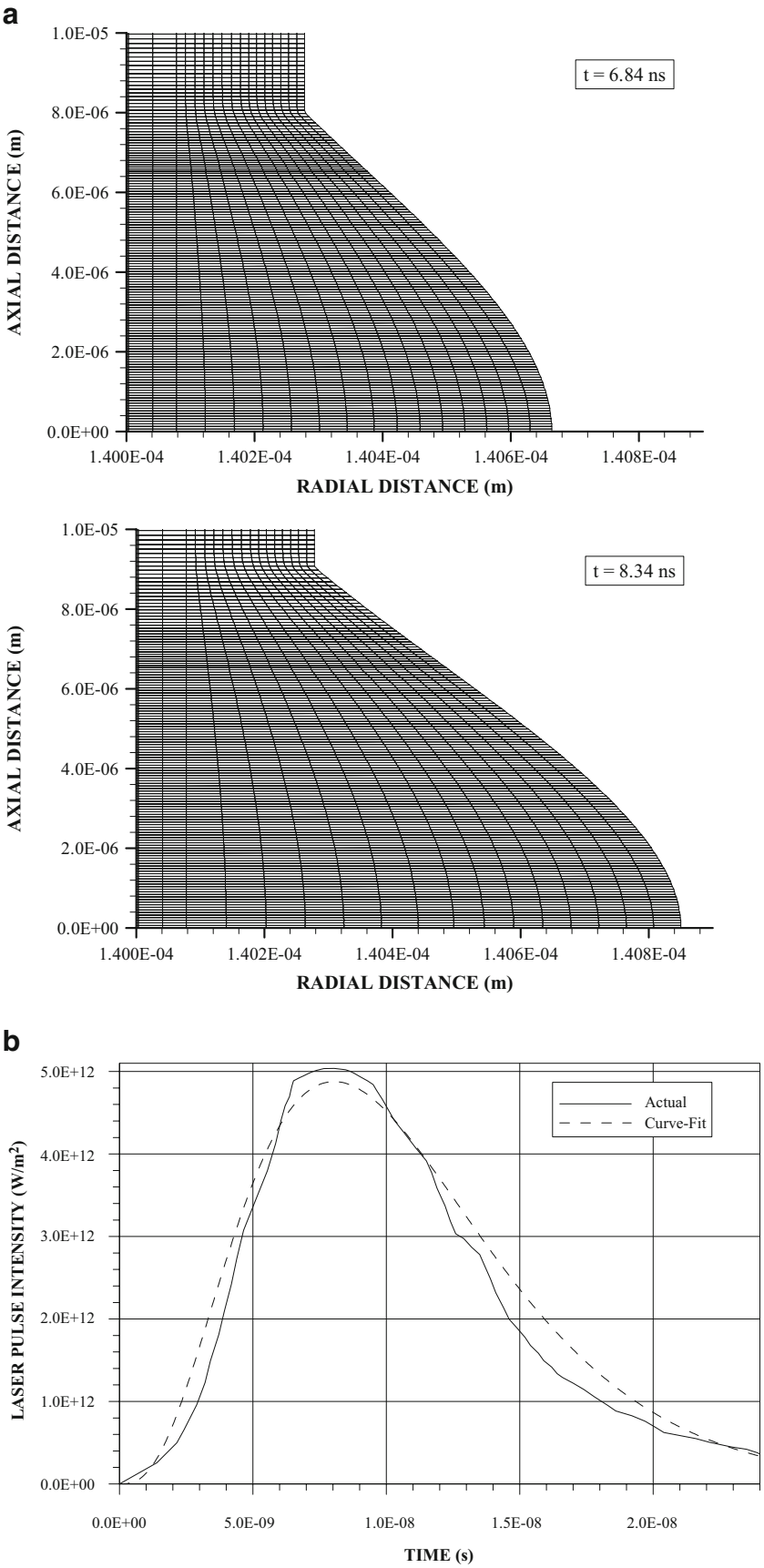

Fig. 2 **a** Moving mesh around the laser-produced cavity for two heating periods and used for vapor front analysis. **b** Temporal variation of laser pulse used in the simulations

positions of the solid–liquid and liquid–vapor interfaces, an implicit scheme is used, i.e., using the initial conditions, the temperature in the whole domain is calculated for the following time steps with the respective conditions.

The calculation domain is divided into grids and a grid independence test is performed for different grid sizes and orientations and the grid size resulting grid-independent solution is used, which is 100×120 mesh points in the r and z-axes (Fig. 1b). A computer program based on implicit scheme is developed to compute the temperature field.

The material properties and pulse intensity used in the simulations are given in Tables 1 and 2, respectively.

5.2 Transiently developing vapor jet (front)

A control volume approach is employed when discretizing the governing equations [18]. A staggered grid arrangement is used in which the velocities are stored at a location midway between the grid points, i.e., on the control volume faces. All other variables including pressure are calculated at the grid points. This arrangement gives a convenient way of handling the pressure linkages through the continuity equation and is known as Semi-Implicit Method for Pressure-Linked Equations (SIMPLE) algorithm. The details of this algorithm are given in [18].

The computer program used for the present simulation can handle a non-uniform grid spacing. Along the radial direction, fine uniform grid spacing is allocated at the inlet (in cavity symmetry axis region) while gradually increasing spacing is considered away from the inlet (in the cavity edge region). Along the axial direction, again fine uniform grid spacing is used inside and near the cavity while the grid spacing gradually increases away from the cavity. The number of grid points in the radial direction is 300 while 215 grid points are used in the axial direction. Since the problem is involved with the moving boundary, the moving meshes are accommodated in the cavity to account for the cavity recession with time. The actual computational grid in the cavity region is shown in Fig. 2a. It should be noted that the evolving of cavity due to recessing towards the solid material during the heating period is accommodated through using the moving meshes in the solution domain. The grid independence test is conducted and grid size (215×300) resulting in grid-independent solution is used in the simulations.

Eight variables are computed at all grid points. These are the two velocity components, local pressure, two turbulence quantities, temperature, and two mass fractions. The properties of substrate material used in the simulations are given in Table 3. The temporal variation of the laser pulse used in the simulations is shown in Fig. 2b. The nominal laser pulse length at full width at half maximum (FWHM) is 24 ns.

6 Elasto-plastic analysis

To investigate the effect of the elastic-plastic wave propagation on the deformation behavior and the distribution of stresses, a commercial non-linear explicit dynamic FE code ANSYS LS-DYNA is used. For modeling purposes, two-dimensional axisymmetric finite element analysis was found out to be adequate. To incorporate the temporal variation in the recoil pressure magnitude and its spatial distribution, the pressure predicted from the solution of momentum equation is used. The time-dependent pressure was applied on the top surface of the cavity. The cavity was meshed using PLANE162 element. PLANE162 is used for modeling 2-D solid structures in ANSYS LS-DYNA. The element can be used either as a planer or as an axisymmetric element. The element is defined by four nodes having six degrees of freedom at each node: translations, velocities, and accelerations in the nodal x and y directions. The element is used in explicit dynamic analyses only.

Material behavior was idealized as strain-rate-dependent isotropic plasticity. In this model, a load curve is used to describe the initial yield strength, so, as a function of effective strain rate. The yield stress for this material model is defined as:

$$\sigma_y = \sigma_0 \varepsilon^t + E_k \varepsilon_p^{\text{eff}}$$

where σ_o is the initial yield strength, ε^t is the effective strain rate, $\varepsilon_p^{\text{eff}}$ is the effective plastic strain, and E_k is given by:

$$E_k = \frac{E_l E_{\tan}}{(E_l - E_{\tan})}$$

where E_l is the modulus of elasticity and $E_{\tan}$ is the tangent modulus for the material. The material properties used to model the constitutive behavior of the steel are E_l= 209 GPa, v=0.29, density=17,850 kg/m^3, and $E_{\tan}$= 2.2 MPa.

Table 3 Properties of water and vapor front used in the simulations

	Water	Vapor front
Density (kg/m^3)	998.2	50, 800
Viscosity (kg/m/s)	0.001003	1.34×10−5
Mass diffusivity (m^2/s)	2.88×10−5	
Specific heat capacity (J/kg/K)	4182	2014
Thermal conductivity (W/m/K)	0.6	0.0261
Molecular weight (kg/kmol)	18.0152	56

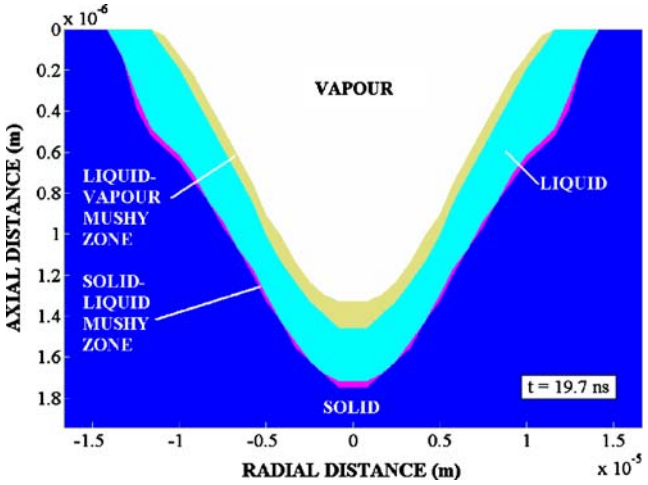

Fig. 3 Cavity shape and phases around the cavity for 19.7 ns of heating duration

7 Results and discussions

Laser-induced shock processing of steel surface is considered. Evaporation and melting during the heating pulse are formulated using the energy method. Recoil pressure generated in the laser-produced cavity is predicted numerically solving the flow and heat transfer equations. The mechanical response of the surface due to impacting load generated by the recoil pressure is examined and the depth of laser-induced shock in the substrate material is predicted. Table 1 gives the properties of the substrate material while Table 2 gives properties of laser pulse used in the simulations.

Figure 3 shows cavity shape at t=19.7 ns of the heating pulse. The presence of mushy zone particularly at the vapor–liquid interface is evident; however, the size of mushy zone at solid–interface is considerably small. This is due to the latent heat of evaporation, which is significantly larger than the latent heat of melting, i.e., energy stored in the vapor–liquid mushy zone at evaporation temperature is larger than that at melting temperature.

Figure 4 shows contours of velocity magnitude while Fig. 5 shows a three-dimensional view of pressure distribution in the cavity for different heating periods. Velocity close to the cavity symmetry axis attains high values due to high rate of mass removal rate along the symmetry axis. It should be noted that recession velocity of the cavity surface along the symmetry axis is higher than that at other radial locations [16]. Some variation in the velocity magnitude at radial location of 1 μm along the

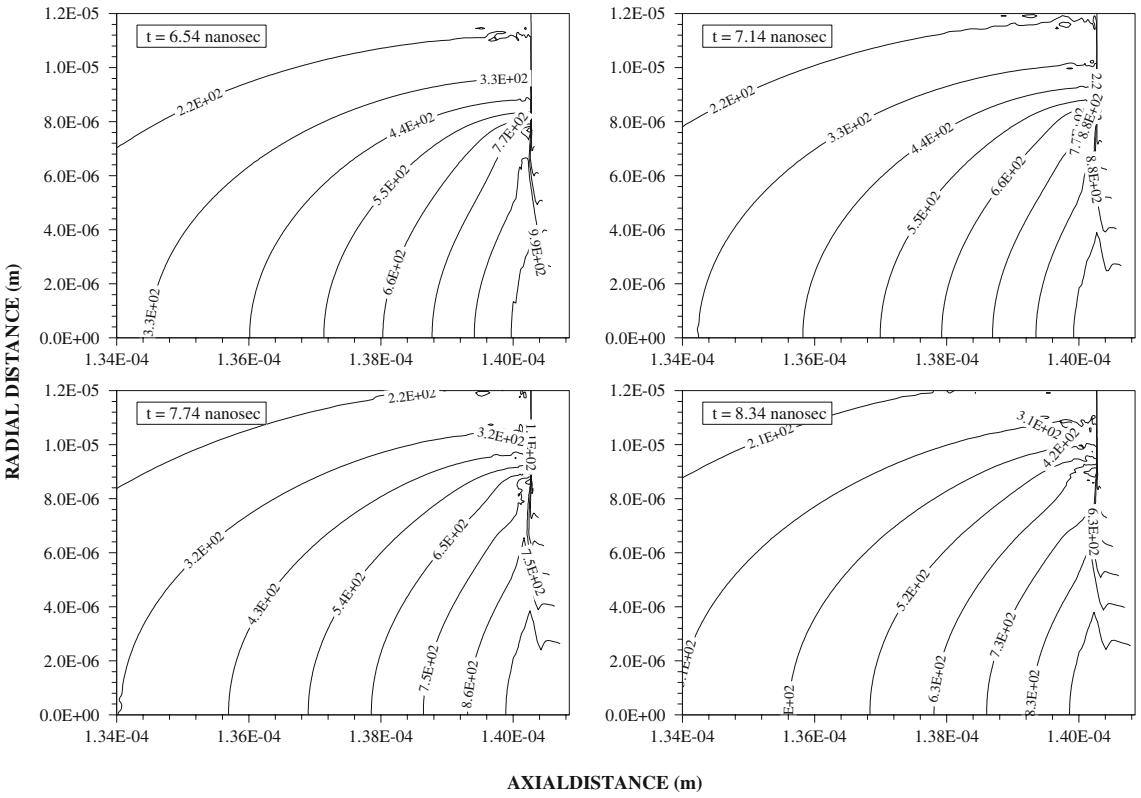

Fig. 4 Velocity contours in the region close to the cavity for different heating periods

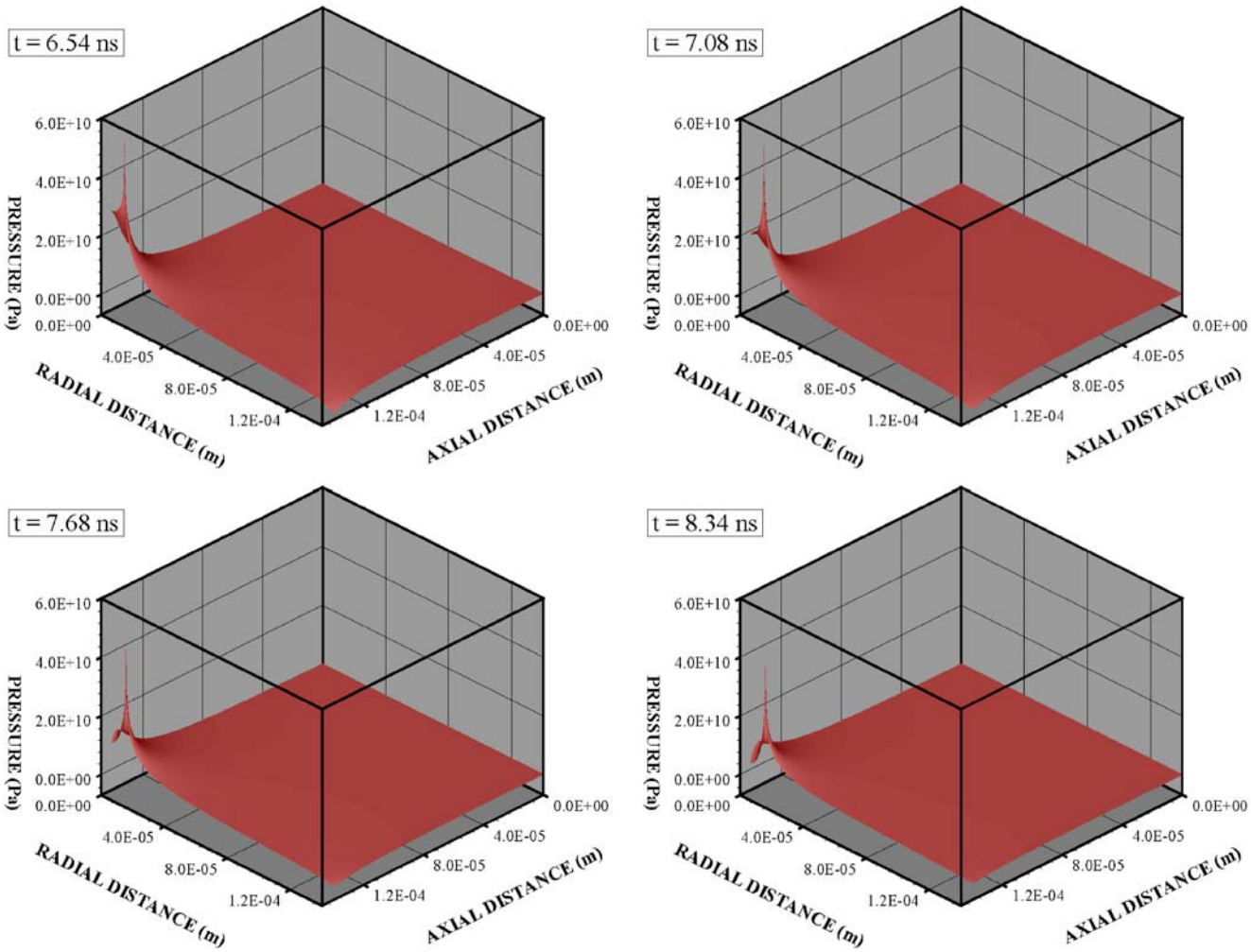

Fig. 5 Three-dimensional view of pressure contours for different heating durations

axial distance is due to rapid expansion of vapor front close to the recessing cavity surface while jet front is expanding into stagnant water. This situation results in complex flow structure in this region, i.e., suppression of jet expansion towards the cavity exit by the stagnant ambient fluid, which is water, and recessing cavity surface towards the solid bulk gives rise to high-pressure vapor to expand radially. This results in pressure rise in the region close to the cavity wall. This situation can also be observed from Fig. 6. The pressure levels in the order of 10 GPa is generated in the cavity. The occurrence of maximum pressure close to the cavity edge is also observed from Fig. 6, in which pressure variation along the axial distance at symmetry axis is shown. Increasing heating duration lowers the recoil pressure in the cavity. This may occur because of one or all of the following: (a) vapor jet penetration into the stagnant water ambient lowers the axial as well as radial momentum of the jet as the time progresses [16], and (b) the cavity size increases, because of the evaporation of the cavity wall due to absorption of the laser beam, and expansion of the jet in the radial as well as axial directions enhances in the cavity lowering the recoil pressure.

Figure 7 shows three-dimensional view of von-Mises stress and plastic strain in the laser-irradiated region for heating period of 7 ns. von-Mises stress attains high values close to the edge of the irradiated region. This is due to the high pressure developed in this region (Fig. 6). Moreover, the region close to the irradiated centre, von-Mises stress becomes slightly less and remains the same along the radial direction. The depth of the high-stress region is more in the region close to the edges of the irradiated spot. This situation is true for all heating periods. Consequently, once the flow field, due to evaporation, is developed in the cavity, the pressure field becomes high in the region of the cavity edge. Since the heating duration is small, convective acceleration of the flow in the cavity is small. Consequently, pressure field developed in the cavity remains almost at the same magnitude, with some small changes, during the heating period.

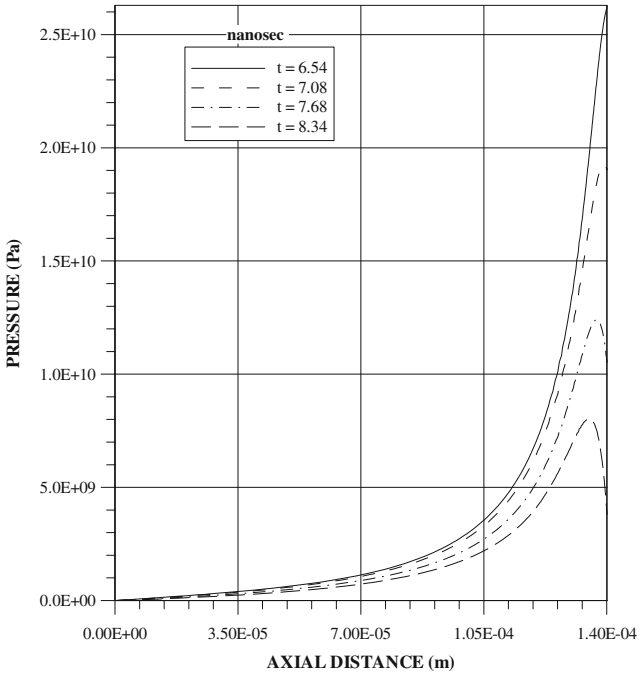

Fig. 6 Pressure distribution along the symmetry axis at different

Figure 8 shows von-Mises plastic strain along the radial direction within the vicinity of the surface for the three heating periods. Plastic strain increases significantly at the edge of the cavity. This increase is almost twice the value at the central region of the cavity. It should be noted that radial location $r=0$ corresponds to the symmetry axis. Moreover, increasing heating period enhances von-Mises plastic strain. This is because of the pressure variation with time, i.e., increasing evaporation rate with time increases the pressure rise in the cavity, particularly in the region of the cavity edge. However, increase in von-Mises plastic strain during the duration of 6 to 8 ns is much higher than that of 8 to 10 ns. This is again due to temporal variation of evaporation and pressure build-up in the cavity, which rises at a fast rate in the early heating period. This situation is also observed from Fig. 9, in which the temporal variation of maximum plastic strain is shown, i.e., the raise of maximum plastic strain is significantly high during the period 6 to 8 ns.

Figure 10 shows temporal variation of depth of maximum plastic strain. The depth of plastic strain corresponds to the depth of plastically deformed zone. The depth of plastic deformation increases gradually up to 3 ns and this increase becomes rapid until 7 ns and it becomes gradual after 8 ns of heating duration. This is mainly because of the temporal variation of evaporation rate and pressure developed in the cavity, which vary significantly with progressing time. The maximum depth of plastic region reaches 20 μm below the surface after 10 ns of heating period. However, this occurs in the region close to the irradiated spot edge. It should be noted that vapor expansion in the radial direction after 8 ns of heating period

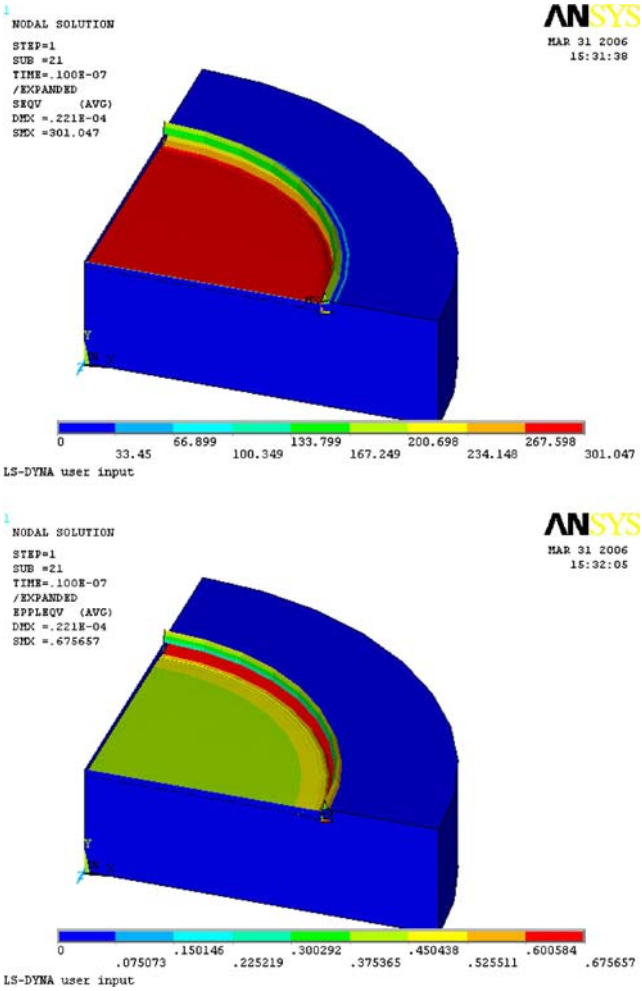

Fig. 7 von-Mises stress and von-Mises plastic strain in the region irradiated by a laser beam

results in gradual rise of pressure in the edge of the cavity. This, in turn, lowers the magnitude of mechanical pressure load and suppressing the rapid enhancement of depth of plastic deformation.

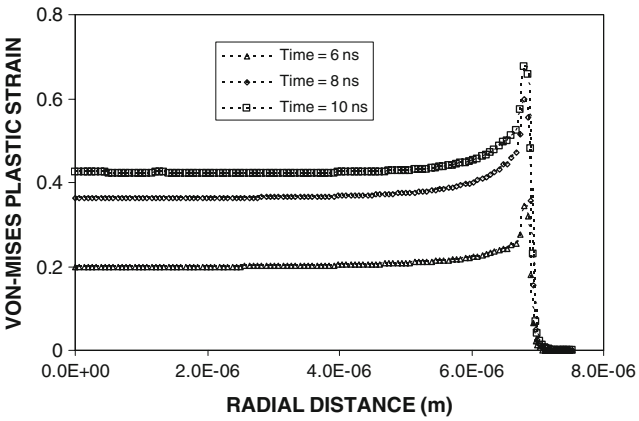

Fig. 8 von-Mises plastic strain in the radial direction at different heating periods

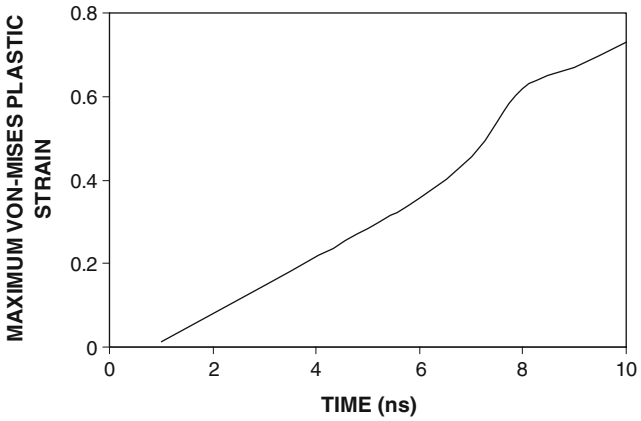

Fig. 9 Temporal variation of maximum von-Mises plastic strain

8 Conclusions

Laser evaporative heating and shock processing of the irradiated surface is examined numerically. Solid heating, melting, and evaporation are modeled using an energy method during the laser-heating pulse. The vapor front expansion from laser-produced cavity and flow field within the cavity are predicted numerically using moving meshes. The pressure developed in the cavity during rapid evaporation is determined numerically and material response to a pressure field is obtained using a finite element method. Since the vapor emanating from the laser-produced cavity expands into ambient water, low density vapor expansion is slowed by its impact into water ambient. This results in a complex flow structure within the cavity. Consequently, radial expansion of the vapor front enhances the pressure increase in the region of cavity edges. Since the rate of evaporation varies with time, pressure build-up in cavity edges also varies with time. Moreover, the impact loading of the surface due to high-pressure results in high level of von-Mises stress. The rate of plastic deformation is high during the heating period of 3–8 ns. The depth of plastically deformed region in the order of 20 μm below the surface occurs after a 10-ns heating period.

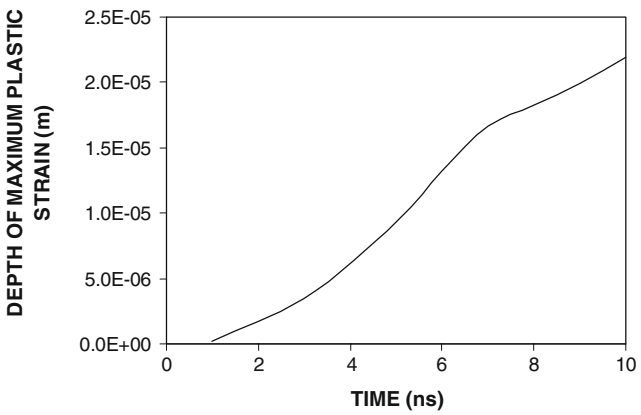

Fig. 10 Temporal variation of location of maximum von-Mises plastic strain in the substrate

9 Nomenclature

a	Gaussian parameter (m)
A	Area (m^2)
a	Gaussian parameter (m)
Cp	Specific heat capacity (J/kg/K)
C	Various empirical constants in turbulence model
$Cp_{1,2,3,4,5}$	Coefficients in the source term
D	Species diffusion coefficient (m^2/s), jet width (m)
E	Energy (J)
E_l	Young's modulus (Pa)
$f(r, t)$	Cavity profile equation
h	Convective heat transfer coefficient ($W/m^2/K$);
h_{vapor}	Enthalpy of vapor (J/kg)
h_{water}	Enthalpy of water (J/kg)
I_0	Laser power intensity (W/m^2)
K	Turbulence kinetic energy (m^2/s^2)
k	Thermal conductivity (W/m/K)
k_t	Turbulent thermal conductivity (W/m/K)
m_m	Mass of liquid phase in the mushy zone (kg)
m_b	Mass of vapor phase in the mushy zone (kg)
L_b	Latent heat of boiling (J/kg)
L_m	Latent heat of melting (J/kg)
Pr	Prandtl number
$\overline{p}$	Time-averaged pressure (Pa)
p'	Fluctuating component of mixture pressure (Pa)
$\overline{p}'$	Pressure correction (Pa)
r	Distance along the radial direction (m)
r_f	Reflectance
S_o	Source term (W/m^3)
Sc	Schmidt number
T	Temperature (K)
$\overline{T}$	Time-averaged temperature (K)
T'	Fluctuating component of temperature (K)
t	Time (s)
t_m	Time at which melting starts in the solid phase (s)
t_{sl}	Time at which solid–liquid mushy zone starts converting into the liquid phase (s)
t_b	Time at which evaporation starts in the liquid phase (s)
U	Energy content (J)
u	velocity component (m/s), z-direction velocity (m/s)
$\overline{u}$	Time-averaged velocity component (m/s), time-averaged z-direction velocity (m/s)

u'	Fluctuating component of z-direction velocity (m/s)
$\overline{u}'$	z-direction velocity correction (m/s)
$\overline{u}^*$	Guessed z-direction velocity (m/s)
$\forall$	Volume (m^3)
V	Velocity (m/s)
v	r-direction velocity (m/s)
$\overline{v}$	Time-averaged r-direction velocity (m/s)
v'	Fluctuating component of r-direction velocity (m/s)
$\overline{v}'$	r-direction velocity correction (m/s)
$\overline{v}^*$	Guessed z-direction velocity (m/s)
x	Quality
x_m	Fraction of mass of liquid phase in the mushy zone.
x_b	Fraction of mass of vapor phase in the mush zone.
Y	Mass fraction in species transport model
$\overline{Y}$	Time-averaged mass fraction in species transport model
z_c	Depth of cavity (m)
z	Distance along the radial direction (m)
z_b	Depth of vapor phase in the axial direction (m)

Greek symbols

δ	Absorption coefficient (1/m)
ε	Rate of dissipation (m^2/s^3)
ε^{eff}	Effective plastic strain
Γ	Diffusion coefficient (kg/m/s)
μ	Molecular viscosity coefficient (kg/m/s)
μ_t	Turbulent viscosity coefficient (kg/m/s)
φ	Arbitrary variable
$[\varphi]$	Unit of arbitrary variable
ρ	Density (kg/m^3)
$\overline{\rho}$	Time-averaged density (kg/m^3)
ρ'	Fluctuating component of density (kg/m^3)
σ_K	Turbulent Prandtl number for K
σ_ε	Turbulent Prandtl number for ε
σ_o	Initial yield strength (Pa)

Subscripts

b	vapor–liquid mushy zone; boiling
eff	effective
m	solid–liquid mushy zone; melting
o	initial value
p	time index
ref	reference
s	solid, surface
t	turbulent
v	vapor

Acknowledgment The authors acknowledge the support of King Fahd University of Petroleum and Minerals, Dhahran, Saudi Arabia, for this work.

References

1. Yilbas BS, Naqavi IZ, Shuja SZ (2002) Modeling and experimental study into the laser-assisted nitriding of Ti–6Al–4V. ASME. J Manuf Sci Eng 124:863–874 doi:10.1115/1.1511171
2. Yilbas BS (2003) Laser shortpulse heating of gold: variable properties case. Int J Heat Mass Transfer 46:3511–3520 doi:10.1016/S0017-9310(03)00131-5
3. Montross CS, Wei T, Ye L, Clark G, Mai YW (2002) Laser shock processing and its effects on microstructure and properties of metal alloy: a review. Int J Fatigue 24:1021–1036 doi:10.1016/S0142-1123(02)00022-1
4. Thorslund T, Kahlen FJ, Kar A (2003) Temperatures, pressures and stresses during laser shock processing. Opt Lasers Eng 39:51–71 doi:10.1016/S0143-8166(02)00040-4
5. Senecha VK, Zhang J, Wang W, Pant HC (2002) Numerical simulation study of laser-driven shock wave propagation in planar aluminium foils. J Phys Condens Matter 14:10917–10920 doi:10.1088/0953-8984/14/44/401
6. Ding K, Ye L (2003) Three-dimensional dynamic finite element analysis of multiple laser shock peening processes. Surf Eng 19 (5):351–358 doi:10.1179/026708403225007563
7. Yin S, Zhang Y, Zhou J, Yang J (2005) Movement control of forming by laser shock wave. Proc SPIE-Int Soc Opt Eng 6043 I, MIPPR 2005: SAR and Multispectral Image Processing
8. Berthe L, Fabbro R, Peyre P, Bartnicki E (1997) Laser shock processing of materials: Experimental study of breakdown plasma effects at the surface of confining water. Proc SPIE-The Int Soc Opt Eng 3097:570–575
9. Chen JP, Ni XW, Lu J, Bian BM, Wang YW (2000) Laser-induced plasma shock wave and cavity on metal surface underwater. Microw Opt Technol Lett 25(5):307–311 doi:10.1002/(SICI)1098-2760(20000605)25:5<307::AID-MOP6>3.0.CO;2-1
10. Faraggi E, Wang S, Gerstman B (2005) Stress confinement, shock wave formation and laser induced damage. Progress in Biomedical Optics and Imaging-Proceedings of SPIE, Vol. 5695, Optical Interactions with Tissue and Cells XVI, 2005, pp. 209–215.
11. Schmidt-Uhlig T, Karlitschek P, Yoda M, Sano Y, Marowsky G (2000) Laser shock processing with 20 MW laser pulses delivered by optical fibres. EPJ Appl Phys 9(3):235–238 doi:10.1051/epjap:2000109
12. Zhang Y, Cai L, Yang J, Ren N (1997) Measurements of laser-induced shock pressures using PVDF transducer. Chin J Lasers B B6(1):81–85 English Edition
13. Yilbas BS, Gondal MA, Arif AMF, Shuja SZ (2004) Laser shock processing of Ti–6Al–4V alloy. Proc I MECH E Part B, J Eng Manuf 218(5):473–482
14. Yilbas BS, Naqavi IZ (2003) Laser heating including phase change process and thermal stress generation in relation to drilling. Proc Instn Mech Engrs Part B: J Eng Manuf 217:977–991
15. Yilbas BS, Naqavi I (2006) Laser heating and thermal stresses time exponentially heating pulse case. Trans Can Soc Mech Eng 30:113–142
16. Mansoor SB (2006) Laser evaporative heating in relation to machining, M.Sc. Thesis, Mech. Eng. Dept., KFUPM
17. Naqavi IZ (2001) Conduction and non-conduction limited laser heating process—mathematical simulation, M.Sc. Thesis, Mech. Eng. Dept., KFUPM
18. Patankar SV (1980) Numerical heat transfer. McGraw-Hill, New York